ACS APPLIED ENERGY MATERIALS

www.acsaem.org Article

Silicon Microreactor as a Fast Charge, Long Cycle Life Anode with High Initial Coulombic Efficiency Synthesized via a Scalable Method

Qianran He, Maziar Ashuri, Yuzi Liu, Bingyu Liu, and Leon Shaw*

Cite This: https://doi.org/10.1021/acsaem.1c00351 Read Online

ACCESS | Metrics & More | Article Recommendations | Supporting Information

ABSTRACT: Applications of silicon as a high-performance anode material have been impeded by its low intrinsic conductivity and huge volume expansion (>300%) during lithiation. To address these problems, nano-Si particles along with conductive coatings and engineered voids are often employed, but this results in high-cost anodes. Here, we report a scalable synthesis method that can realize high specific capacity (~800 mAh g^{-1}), ultrafast charge/discharge (at 8 A g^{-1} Si), and high initial Coulombic efficiency (~90%) with long cycle life (1000 cycles) at the same time. To achieve 1000 cycle stability, micron-sized Si particles are subjected to high-energy ball milling to create nanostructured Si building blocks with nano-channel-shaped voids encapsulated inside a nitrogen (N)-doped carbon shell (termed as Si microreactor). The nanochannel voids inside a Si microreactor not only offer the space to accommodate the volume expansion of Si but also provide fast pathways for Li-ion diffusion into the center of the nanostructured Si core and thus ultrafast charge/discharge capability. The porous N-doped carbon shell helps to improve the conductivity while allowing fast Li-ion transport and confining the volume expansion within the Si microreactor. Submicron-sized Si microreactors with a limited specific surface area (35 m^2 g^{-1}) afford sufficient electrode/electrolyte interfacial area for fast lithiation/delithiation, leading to the specific capacity ranging from ~800 to 420 mAh g^{-1} under ultrafast charging conditions (8 A g^{-1}), but not too much interfacial area for surface side reactions and thus high initial Coulombic efficiency (~90%). Since Si microreactors with superior electrochemical properties are synthesized via an industrially scalable and eco-friendly method, they have the potential for practical applications in the future.

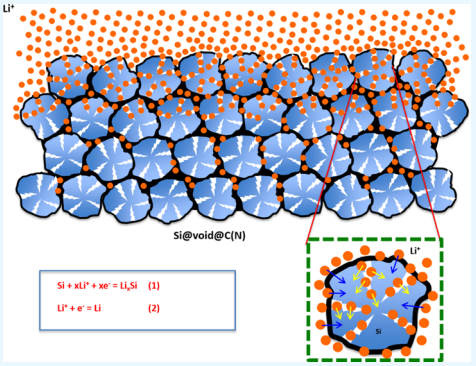

KEYWORDS: *silicon anodes, Li-ion batteries, fast charge, scalable synthesis, high capacity*

1. INTRODUCTION

As the past decades witnessed the revolution of smartphones and the soar of mobile internet, it is believed that the following revolution is coming with electric vehicles playing a major role in the construction of smart city and internet of things (IoT). Integrated with techniques of artificial intelligence (AI) and cloud computing, electric vehicles as well as other consumer electronic devices are also acting as the terminals of data generation and processing, causing high energy consumption and urgent demand for lithium-ion batteries (LIBs) that need to have high energy density, fast charging capability, as well as low fabrication cost and long cycle life.[1−3] Si as one of the most promising anode materials for the next generation LIBs has attracted tremendous attention and investigation due to its extremely high specific capacity (3579 mAh g^{-1} for $Li_{15}Si_4$, which is about 10 times of graphite's specific capacity), low lithium-alloying voltage (0.22 V vs Li/Li^+, a safer potential to avoid undesirable Li plating comparing with graphite), and abundant amount on earth.[4−6] However, the low intrinsic conductivity of Si (~10^{-6} S cm^{-1}) and the huge volume expansion (>300%) during lithiation have hindered the direct application of Si as a high-performance anode material. In particular, the extreme volume change, which causes mechanical fracture of the electrode, loss of interparticle contact, as well as repeated solid electrolyte interphase (SEI) layer formation and collapses that deteriorate the electrolyte, is extremely detrimental and has resulted in fast capacity decay and poor electrochemical performance.[4−7]

Various strategies have been applied to address the volume expansion issue of Si anodes. Most of the effective solutions come from structure and geometry designs,[6] including: (1) particle-based structures (such as solid core−shell nanoparticles,[8,9] hollow core−shell nanoparticles,[10,11] and yolk−shell nanoparticles,[12−19]); (2) porous Si structures (i.e., nano-sized porous Si structures[20,21] and micron-sized porous Si structures);[22,23] and (3) one-dimensional structures (Si nanowires/nanorods,[4,24,25] Si nanotubes,[26,27] Si nanofib-

Received: February 2, 2021
Accepted: April 8, 2021

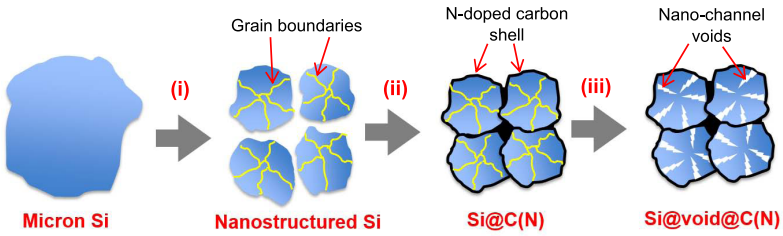

Figure 1. Schematic of the three major synthesis steps for making Si@void@C(N) powder as the anode material of Li-ion batteries: (i) high-energy ball milling, (ii) carbonization treatment, and (iii) partial etching of the Si core.

ers).[28−30] These explorations and efforts have made great progress, significantly improving the Si anode structure stability and electrochemical performance. However, a large number of designs have heavily relied on the use of Si nanoparticles[8−18] to alleviate the massive volume change, which also brings in high specific surface area, causing a large amount of undesired side reactions and thus leading to low initial Coulombic efficiency (ICE). In addition, the cost of Si nanoparticles is significantly higher than that of micrometer-sized Si particles (about 5−10 times more expensive), making commercial applications of Si-nanoparticle-based anodes cost prohibitive. Furthermore, many yolk−shell nanostructures are generated with the use of environmentally unfriendly hydrofluoric acid (HF) solution,[12,14,15,17−19] which makes the processing cost high because of the special precaution required during processing and wastewater treatment. In spite of these challenges, it is encouraging to see several works in recent years utilizing micron-sized or unique designs to avoid the use of Si nanoparticles with reported breakthroughs on high mass loading and ICE larger than 90%.[30−33] Recently, Si nanoparticles have been added to Li−C microspheres to decrease the polarization for Li plating/stripping of the Li−C electrode while increasing the specific capacity of the Li−C microspheres at the same time.[34] This work has expanded Si functions from as the primary Li-ion storage anode to as the additive to enhance the electrochemical performance of Li anodes.[34]

Here, we report a scalable synthesis method that can produce Si/C composite anodes without resorting to the use of Si nanoparticles and HF etchant while realizing high ICE, fast charge/discharge, and long cycle life at the same time. We designed and successfully synthesized a Si/C composite with an in situ nitrogen (N)-doped carbon shell and internal nanochannel void structure, denoted as Si@void@C(N) microreactor which can achieve 91% Coulombic efficiency at the first cycle and deliver 1100, 1000, 900 and 800 mAh g^{-1} of Si specific capacity at the current density of 2, 4, 6, and 8 A g^{-1}, respectively. Furthermore, the battery could live up to 1000 cycles under 8 A g^{-1} current density while still providing a higher specific capacity than the state-of-the-art carbonaceous anodes. The synthesis method includes three major steps (Figure 1): (1) high-energy ball milling that breaks down micron-sized Si particles to submicron-sized particles with nanograins (i.e., forming nanostructured Si particles), (2) carbonization process that embeds submicron-sized nanostructured Si particles in a porous carbon framework with in situ nitrogen (N) doping to form Si@C(N), and (3) NaOH etching treatment to introduce engineered voids with nanochannel morphology inside the carbon-encapsulated nanostructured Si core, leading to the formation of Si@void@C(N). This synthesis method (patent pending) is facile, low cost, and scalable because it starts with low-cost micron-sized Si particles and uses industrially scalable high-energy ball milling to form a large quantity of nanostructured Si particles, followed by a carbonization treatment to produce Si@C(N) and finalized by eco-friendly NaOH chemical etching to create nanochannel voids inside the Si@C(N) composite to form Si@void@C(N) microreactor particles. Each of these Si@void@C(N) particles with sizes ranging from 0.1 to ∼1.0 μm (see Figure S1) serves as a microreactor to accommodate the volume expansion and shrinkage within the microreactor during lithiation and delithiation without inducing much volume change of the microreactor itself, while the outer carbon framework offers high electronic conductivity. Equally important, the nanochannel voids also permit fast Li-ion transport inside the microreactor so that fast charging can be done without Li plating. Detailed material characterization and electrochemical analysis of these Si@void@C(N) microreactors will be discussed below to illustrate the mechanisms of how Si microreactors can achieve high ICE and fast charge capability with long cycle life simultaneously.

2. RESULTS AND DISCUSSION

2.1. Synthesis of Si@void@C(N) Nanostructures. The starting material of this study is micron-sized Si particles, instead of commercial Si nanoparticles that were used in many studies.[8−18] As a result, the raw material cost is less than 10% of Si nanoparticles, significantly improving the perspective of the industry-scale application of the method and material reported in this study. After high-energy ball milling, the carbon framework to encapsulate submicron-sized nanostructured Si particles is formed through carbonization of a carbon precursor containing nitrogen element (i.e., polyacrylonitrile (PAN)) at 900 °C. This carbonization treatment produces the N-doped carbon framework in situ while forming SiC nanocrystallites at the Si/C interface (to be detailed later). These synchronized results are highly related to the ball milling process before the carbonization treatment (see the Experimental Section). The high-energy ball milling not only breaks down the size of micro-Si particles into submicron-sized, nanostructured Si particles (Figure S1) but also brings in fresh surfaces, dangling bonds, structural defects, and grain boundaries.[34−37]

2.2. X-ray Diffraction (XRD), Raman, and X-ray Photoelectron Spectroscopy (XPS) Characterizations. As shown in Figure 2a, the ball-milled Si powder exhibits significant peak broadening in comparison to the X-ray diffraction (XRD) pattern of the starting micro-Si powder, giving an average size of Si crystallites at ∼160 nm estimated using the Debye−Scherrer equation[34] and thus confirming that high-energy ball milling has led to the formation of nanostructured Si powder. Because of the mechanical activation induced by high-energy ball milling at room

https://doi.org/10.1021/acsaem.1c00351
ACS Appl. Energy Mater. XXXX, XXX, XXX−XXX

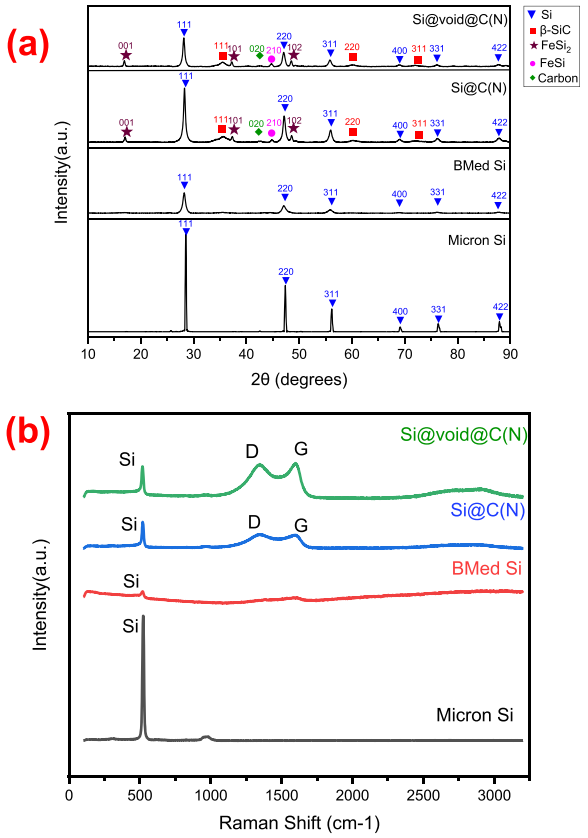

Figure 2. (a) XRD patterns of Si-based materials after different synthesis steps, including micron Si before high-energy ball milling, ball-milled Si (BMed Si), ball-milled Si after carbonization treatment (Si@C(N)), and the final microreactor after etching (Si@void@C(N)); (b) Raman spectra of Si-based materials after different synthesis steps, as indicated.

temperature,[34−37] the energy barrier of chemical reactions has been reduced so that a small amount of β-SiC (JCPDS #29-1129) can form at 900 °C (see Figure 2a), rather than at 1400 °C or higher typically required for SiC formation.[35−37] The SiC nanocrystallines embedded at the Si/C interface are not continuous (see transmission electron microscopy (TEM) analysis later) and thus not expected to confine Si volume expansion and shrinkage in the charge/discharge process. A small amount of FeSi (JCPDS #89-7376) and $FeSi_2$ (JCPDS #35-0822) are also found to be present in the Si@C powder. These compounds are due to the reaction between the Si powder and the Fe debris from the steel balls used in high-energy ball milling. These compounds, however, may serve as conductive and elastic buffering phases to improve the conductivity and structural integrity of Si anodes, as discussed in refs 38, 39. Finally, a tiny XRD peak at 42.5° is present in the Si@C(N) and Si@void@C(N) powders and is believed to be the major peak of carbon (JCPDS #54-0501).

Raman spectra as shown in Figure 2b have confirmed the existence of carbon after the carbonization treatment. Besides the peak at 520 cm^{-1} coming from Si, two broad peaks at around 1340 and 1590 cm^{-1} correspond to the D band (disordered carbon) and G band (graphitic carbon), respectively. The intensity ratio I_D/I_G is about 97%, suggesting that amorphous disordered carbon and graphitic crystalline carbon exist with a 1:1 ratio in Si@C(N). After etching, the relative intensity of Si peak in comparison with the D band and G band has decreased, consistent with the fact that partial Si has been etched away in the chemical etching process to produce Si@void@C(N) powder. Note that no SiC peaks were detected in the Raman spectrum due to its limited amount and relatively low intensity compared with C in Si@void@C. This is consistent with a previous study[40] showing that SiC peaks can hardly be detected in the Raman spectrum

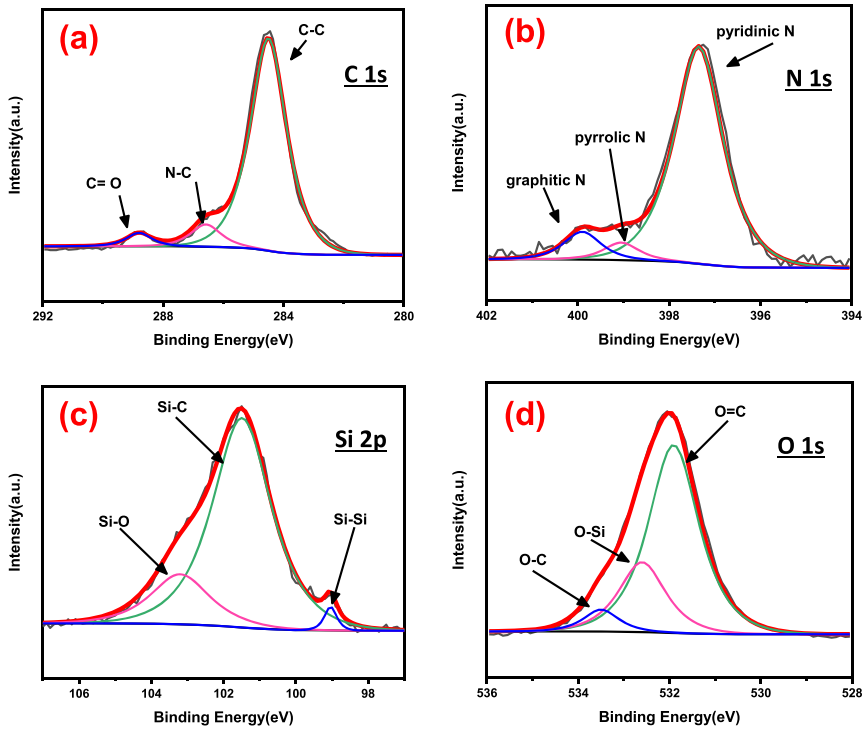

Figure 3. XPS spectra of Si@void@C(N) powder: (a) C 1s, (b) N 1s, (c) Si 2p, and (d) O 1s.

https://doi.org/10.1021/acsaem.1c00351
ACS Appl. Energy Mater. XXXX, XXX, XXX−XXX

when the C concentration is only 7.5 wt % while the concentration of SiC is 92.5 wt %.

X-ray photoelectron spectroscopy (XPS) is utilized to identify the chemical nature of the Si@void@C(N) surface. As shown in Figure 3, the C 1s spectrum reveals the existence of the N−C peak at 286.6 eV,[40] which suggests the N doping to the carbon framework. The N 1s spectrum further indicates the doping positions of the N atoms. The three peaks at a binding energy of 397.3, 399.0, and 399.9 eV corresponds to the pyridinic N (located at the edges of the six-membered aromatic ring), pyrrolic N (located at the edges of the five-membered aromatic ring), and graphitic N (substituted for carbons within the graphene structure) sites.[41] It is believed that pyridinic N- and pyrrolic N-doped carbon can deliver a higher lithium intercalation rate, while graphitic N helps to improve the electronic conductivity of carbon.[42,43] In the Si 2p spectrum, the peaks at 99.0, 101.5, and 103.2 eV correspond to Si−Si, SiC, and SiO_x, respectively, confirming the SiC existence at the surface region of Si@void@C(N). Note that the intensity of the Si−Si peak is relatively small in comparison to that of Si−C and Si−O peaks because the bulk Si is beneath the carbon coating layer and there is slight oxidation of the Si surface during NaOH chemical etching. Furthermore, all sample handling in this study was carried out in air except high-energy ball milling and carbonization processes. As a result, slight oxidation of the Si surface is inevitable. The O−Si peak from the O 1s spectrum also indicates the existence of SiO_x at the surface.

2.3. Scanning Electron Microscopy (SEM), Energy-Dispersive Spectroscopy (EDS), and Brunauer−Emmett−Teller (BET) Characterizations. As mentioned previously, scanning electron microscopy (SEM) investigation (Figure S1) has revealed that high-energy ball milling has reduced micro-Si particles from 5 to 10 μm to submicron-sized, agglomerated particles with sizes ranging from 0.3 to 1 μm. These agglomerated particles are in fact made of primary particles of 100−200 nm. After the carbon coating treatment, the size of agglomerated particles appears to increase slightly to the range of ∼0.3−2 μm. However, no discernable size change is observed after chemical etching, suggesting that chemical etching of Si takes place inside the carbon shell of the Si@C(N) particles. This observation is in good accordance with our experimental design and expectation.

Although SEM observation shows little or no change in the particle size in carbonization treatment and the chemical etching process, the specific surface area (SSA) measurement using the Brunauer, Emmett, and Teller (BET) method has provided valuable insights not accessible through SEM analysis. As shown in Table 1, high-energy ball milling has increased the SSA of Si particles from 1.23 to 13.54 $m^2\ g^{-1}$, consistent with the particle size reduction observed using SEM discussed above. After carbonization treatment, the SSA of Si@C(N) has further increased to 20.28 $m^2\ g^{-1}$, clearly indicating that the carbon shell is porous. The porous nature of the carbon shell makes the partial etching of the nanostructured Si core by a NaOH-based solution possible, leading to a further increase in the SSA of Si@void@C(N) to 35.18 $m^2\ g^{-1}$. Interestingly, as the SSA increases after each synthesis step, the Barrett, Joyner, and Halenda (BJH) pore volume also increases after each synthesis step (Table 1), unambiguously revealing that mesopore volume has increased after high-energy ball milling, then carbonization treatment, and finally chemical etching. Introducing voids inside the Si microreactor could accommodate Si volume expansion during lithiation and improve the structural stability of the Si anode. Note that longer etching time and higher etching temperature could result in a larger amount of Si being removed from the microreactor, thereby producing a higher level of voids. However, such etching conditions will also lead to SiO_x formation in the final Si@void@C(N) product. This is not the desired outcome because the specific capacity offered by SiO_x is significantly lower than that of Si.[44] Thus, etching optimization is required to provide a high specific capacity of the Si@void@C(N) microreactor. Note that the SSA of 35.18 $m^2\ g^{-1}$ for Si@void@C(N), although not fully optimized yet in this study, is lower than the SSA (57 $m^2\ g^{-1}$) of Si nanoparticles used for the comparison investigation in this study (see Figure S5). Because of this lower SSA, the Si microreactor is able to reduce the formation of the SEI layer and thus has a higher first-cycle Coulombic efficiency as will be discussed later.

Table 1. BET and BJH Summary

sample ID	SSA ($m^2\ g^{-1}$)	pore volume (cc g^{-1})
micron Si	1.227	0.003
BMed Si	13.542	0.063
Si@C(N)	20.28	0.095
Si@void@C(N)	35.18	0.177

As revealed through XRD, Raman, and XPS analyses, there are co-presence of multiphases in Si@void@C(N). To estimate the quantity of Si in Si@void@C(N), energy-dispersive spectroscopy (EDS) is employed. Table 2 lists the elemental analysis results derived from the EDS analysis before and after etching. The EDS data indicates that there is 68.11 wt % of Si in Si@C(N) and 49.7 wt % of Si in Si@void@C(N). Since the carbon amount remains unchanged before and after etching, the weight percent increase in the carbon content is mainly due to the weight decrease in the Si content during chemical etching. Assuming that other components (such as SiC, FeSi, $FeSi_2$, and SiO_x) also remain constant during etching like carbon, then it can be estimated that ∼54% of Si has been etched away, leading to 49.7 wt % Si in Si@void@C(N). Table 2 also shows the presence of the N element, which is due to the N-doped carbon shell derived from PAN and confirmed from the XPS analysis. Based on the EDS data, the N concentration in the N-doped carbon shell is about 9 wt %.

Table 2. Element Analysis Results Derived from the EDS

wt %	Si@C(N)	Si@void@C(N)
C	23.44	37.89
N	2.44	4.10
O	6.62	8.63
Si	66.45	47.74
Fe	1.05	1.80
total	100.00	100.00

2.4. TEM, Scanning Transmission Electron Microscopy (STEM), and Elemental Mapping Characterizations. The creation of nano-channel-shaped voids in Si@void@C(N) is achieved via preferential etching of Si grain boundaries inside Si@C(N) particles. Transmission electron microscopy (TEM) images in Figure 4a,b compare the morphologies and mass contrasts of Si@C(N) and Si@

https://doi.org/10.1021/acsaem.1c00351
ACS Appl. Energy Mater. XXXX, XXX, XXX−XXX

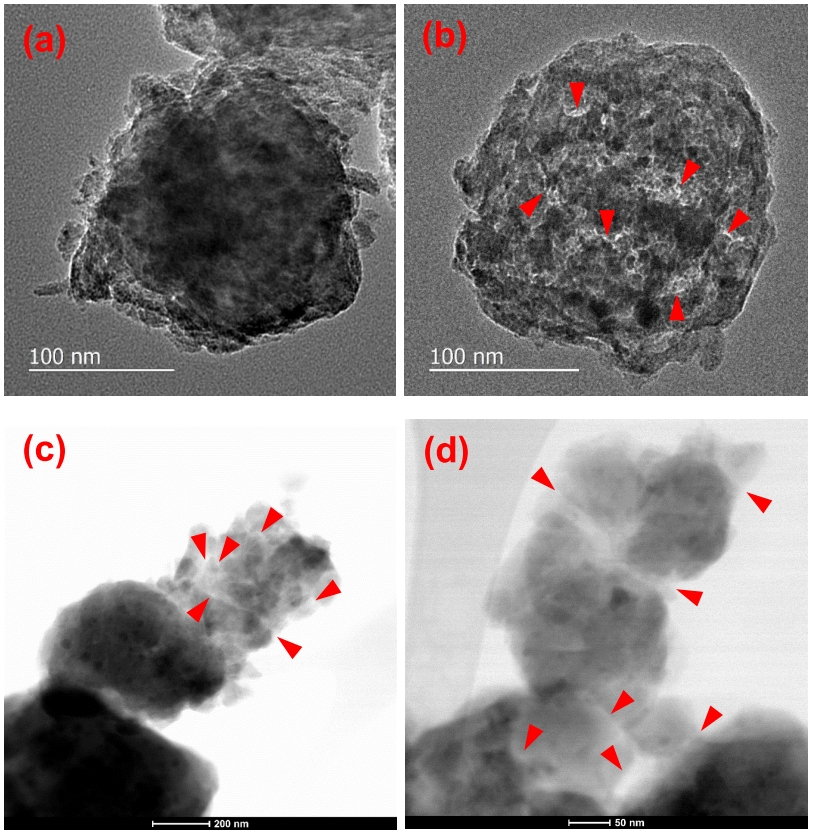

Figure 4. TEM images of (a) a Si@C(N) particle and (b) a Si@void@C(N) particle, and STEM images of (c) several Si@void@C(N) particles and (d) a Si@void@C(N) particle. The arrows in (b–d) indicate some nano-channel-shaped voids inside Si@void@C(N) particles. For clarity, not every nanochannel void is indicated by the arrows.

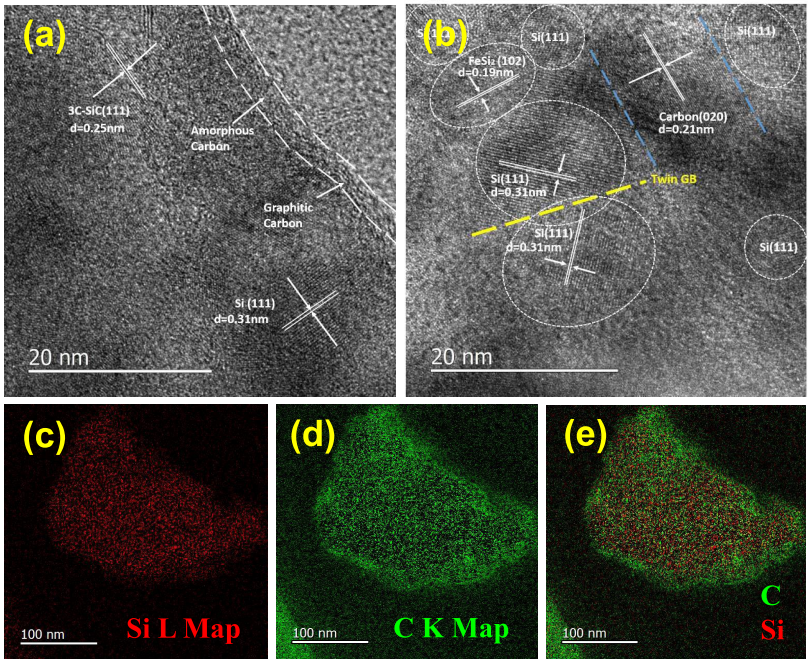

Figure 5. High-resolution TEM images of (a) the edge of a Si@void@C(N) particle and (b) the interior of a Si@void@C(N) particle; and TEM elemental mapping of a Si@void@C(N) particle with (c) Si L map, (d) C K map, and (e) combined map of Si and C elements (color code: red—Si and green—C).

void@C(N) particles. The white areas indicated by red arrows in Figure 4b means that there are fewer materials and more electrons that can pass through those areas. In contrast, there is no this kind of area in Figure 4a because the electron beam cannot pass through the dense particle. This comparison reveals that the Si@void@C(N) particle is porous after etching

https://doi.org/10.1021/acsaem.1c00351
ACS Appl. Energy Mater. XXXX, XXX, XXX−XXX

treatment. To further confirm the presence of voids inside Si@void@C(N) particles, scanning transmission electron microscopy (STEM) was also utilized to image Si@void@C(N) particles. As shown in Figure 4c,d, the voids inside Si@void@C(N) take on nanochannel shape. These nano-channel-shaped voids are produced owing to the preferential etching along the Si grain boundaries inside the nanostructured Si particles generated during high-energy ball milling. It is well documented that high-energy ball milling can produce nanostructured particles of many materials, leading to significant structural defects and grain boundaries inside the ball-milled particles.[34−37] These grain boundaries are thermodynamically and chemically very active and thus can be etched away first in the etching process, creating nanochannel voids rather than conventional spherical voids or bulky voids between the Si core and the outer carbon shell, such as those observed in the yolk−shell structure.[12−19]

High-resolution TEM analysis of Si@void@C(N) particles (Figure 5) further confirms the XRD analysis and offers additional information on the locations of various phases and their crystallinity. As shown in Figure 5a, a thin layer (~5 nm) of carbon coating, identified as a mixture of disordered carbon and graphitic carbon, is present at the surface of the Si@void@C(N) particle, and 3C−SiC (111) crystal lattice is found near the surface of the particle. Many Si (111) crystalline domains with the interplanar spacing d = 0.31 nm can be easily identified inside the Si@void@C(N) particle. In addition, crystal lattice with the interplanar spacing of 0.19 nm, corresponding to the $FeSi_2$ (102) plane, has been identified which is in good accordance with the XRD analysis.

To further corroborate the presence of a carbon shell, elemental mapping of Si@void@C(N) particles has been conducted using an energy-filtered TEM (EFTEM). As shown in Figure 5c−e, a carbon-rich surface of ~5 nm is clearly present in a Si@void@C(N) particle. Since the mapping is done in a transmission mode (3D projection), both carbon and silicon appear to distribute uniformly inside the carbon-rich surface.

2.5. Electrochemical Charge/Discharge Properties. The electrochemical properties of Si@void@C(N) are investigated using half cells in coin cell format with a Li foil as the counter electrode. Figure 6a shows the cyclic voltammetry (CV) curves of a Si@void@C(N) half cell scanning from 0.01 to 1.5 V at a scan rate of 0.5 mV s^{-1}. The first lithiation process of the CV experiment starts from the open-circuit voltage (~2.5 V vs Li/Li^+) to 0.01 V, with two broad peaks at 0.5−0.8 and 1.2−1.4 V ranges corresponding to the decomposition of ethylene carbonate (EC)/diethyl carbonate (DEC) and fluoroethylene carbonate (FEC)/vinylene carbonate (VC), respectively.[45,46] The FEC/VC additives in the electrolyte that are reduced at higher potentials prior to EC/DEC could introduce a different pathway of SEI layer formation, which is more uniform and homogeneous and can prevent further electrochemical reduction of the electrolyte.[47,48] The last broad peak between 0.01 and 0.25 V in the cathodic scan is related to alloying of Si with Li forming Li_xSi, while the anodic peaks at 0.38 and 0.56 V are the step dealloying from highly lithiated Si to less lithiated Si, and finally to Si. The broad peaks at 0.5−0.8 and 1.2−1.4 V disappear in the subsequent cathodic scans, indicating that most of the SEI layer formation takes place in the first scan. Additionally, the peak current increases as the cycle number

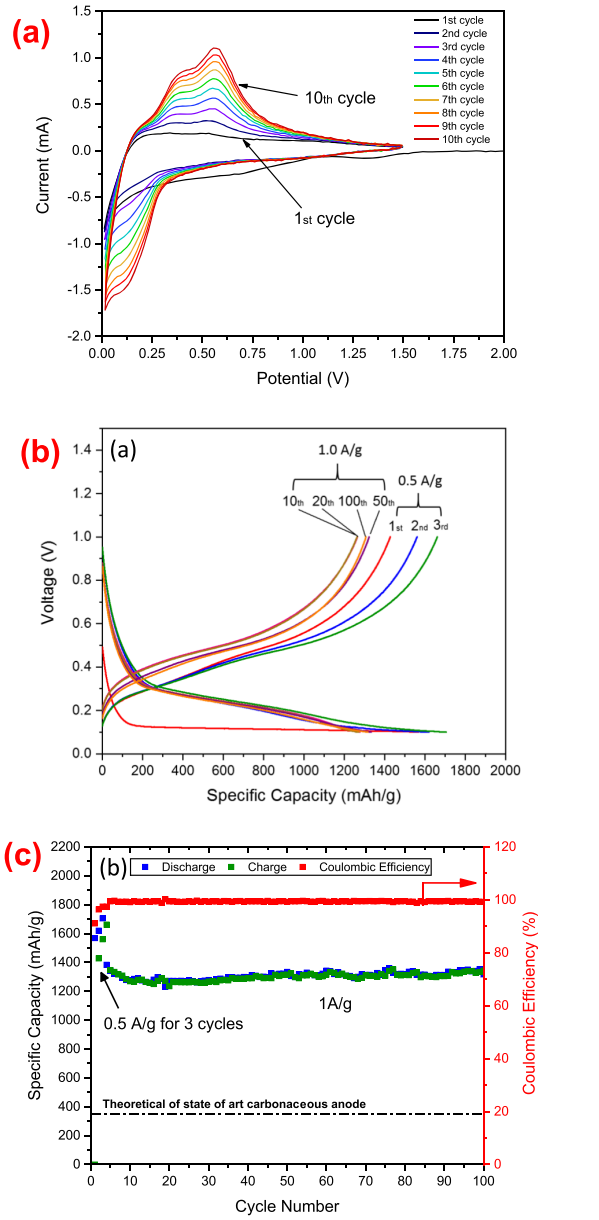

Figure 6. (a) Cyclic voltammogram of Si@void@C(N) half cells from 0.01 to 1.5 V at the scanning rate of 0.5 mV s^{-1} for 10 cycles; (b) voltage profile and (c) specific capacity vs cycle number of Si@void@C(N) half cells charged/discharged at 0.5 A g^{-1} for the first 3 cycles and then 1 A g^{-1} for the following cycles.

increases because of the activation process of the electrode material, which is consistent with other similar studies.[49−51]

The electrochemical performance of Si@void@C(N) half cells is evaluated using constant current chronopotentiometry for 100 charge/discharge cycles as shown in Figure 6b,c. The first three cycles are performed at the current density of 0.5 A g^{-1} Si and the following cycles are at 1.0 A g^{-1} Si. Figure 6b is the voltage profile of selected cycles of Si@void@C(N) half cells. The charge/discharge voltage window is limited to the range between 0.1 and 1.0 V to avoid the formation of $Li_{15}Si_4$ and thus minimize the volume change during lithiation.[52,53] The first discharge process (lithiation) exhibits a long plateau at about 0.1 V corresponds to the formation of not only the amorphous Li_xSi but also the SEI layer. The latter results in extra Li-ion consumption and thus low initial Coulombic

https://doi.org/10.1021/acsaem.1c00351
ACS Appl. Energy Mater. XXXX, XXX, XXX−XXX

efficiency (ICE). The first discharge (lithiation) capacity is 1568 mAh g^{-1} Si, while the first charge (delithiation) capacity gives 1428 mAh g^{-1} Si, leading to a CE of 91%. This ICE is much higher than most other ICE reported for Si anodes (50–80%).[54,55] We have attributed this improvement in the ICE to the unique design of the Si@void@C(N) structure that embeds Si nanoclusters in the N-doped carbon framework, resulting in a relatively low SSA for Si@void@C(N) particles (35.18 m^2 g^{-1} from BET) and thus a significant reduction in the formation of SEI layer at the surface. This structural design also affords high Coulombic efficiency (100%) after 5 cycles (Figure 6c), indicating no discernable SEI layer formation beyond 5 cycles.

Figure 6b also shows an interesting phenomenon, i.e., the second and third cycles at 0.5 A g^{-1} provide higher specific capacities than the first cycle, which is consistent with the previous CV curves showing increasingly larger cathodic and anodic peaks as the cycle number increases. This phenomenon is believed to be the activation of more electrode material as electrolyte penetrates deeper into the electrode during lithiation.[56,57] Interestingly, a similar ramp-up pattern has been observed in the later cycles at 1.0 A g^{-1}. Specifically, the specific capacity at the 50th and 100th cycles are higher than those at the 10th and 20th cycles. This trend can be better observed in Figure 6c from which one can see that as the current density is increased at the 4th cycle, the specific capacity drops first from ~1680 to 1346 mAh g^{-1} and continuously decreases to 1235 mAh g^{-1} at the 19th cycle. However, the specific capacity recovers gradually back to 1323 mAh g^{-1} at the 50th cycle and ends up as 1314 mAh g^{-1} at the 100th cycle. This interesting behavior allows the Si@void@C(N) electrode to maintain its specific capacity with little or no degradation over several hundreds of charge/discharge cycles (Figures 6–8). Furthermore, this behavior does not occur in either commercial Si-nanoparticle electrode or intermediate product Si@C(N) electrode (Figure 7), indicating that this interesting and important phenomenon is due to the unique design of the Si@void@C(N) structure. We believe that this phenomenon occurs because more Si in Si@void@C(N) becomes available for lithiation as the number of cycles increases. Furthermore, this phenomenon is the outcome of two competing mechanisms as explained below.

It is well known that the specific capacities of most electrodes drop when the rate of current increases. This is true for all of the three different Si electrodes measured in this study (Figure 7). One of the reasons for this sudden decrease in the capacity is due to the polarization associated with the IR drop. In some cases, the concentration polarization may also contribute to this sudden capacity drop. After the increase in the rate of current, however, both the commercial Si-nanoparticle electrode and Si@C(N) electrode continue to exhibit decreases in the capacity as the number of cycles increases. This trend is likely related to the repeated fracture and formation of SEI layers[6] and thus the significant increase in impedance as nano-Si and Si@C(N) particles expand and shrink during lithiation and delithiation. In contrast, the Si@void@C(N) electrode displays a gradual increase in the capacity after the jump in the current rate because Si@void@C(N) particles themselves have very limited volume expansion and shrinkage during lithiation and delithiation, thereby a stable SEI layer and gradual but limited increase in impedance (to be shown later). In addition, because of the unique design of Si@void@C(N), another mechanism is likely to operate

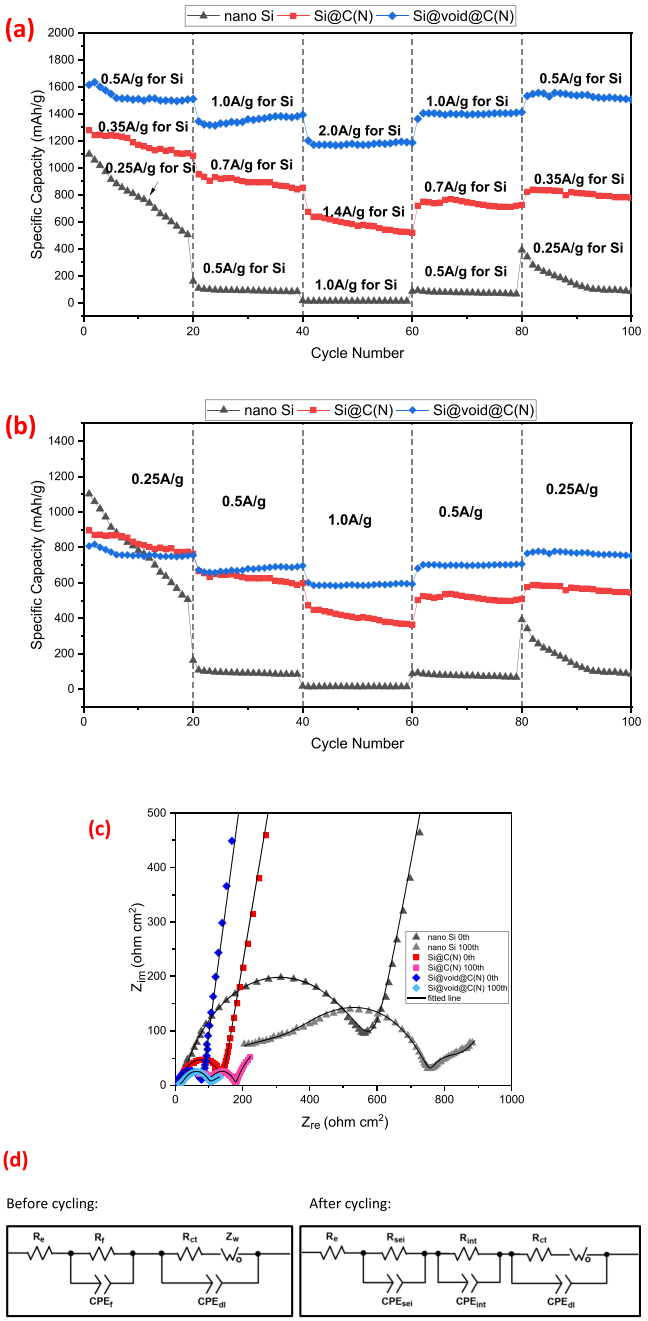

Figure 7. Rate performance comparison among the Si nanoparticle, Si@C(N), and Si@void@C(N) coin cells: (a) specific capacity normalized by the Si mass only as a function of cycle number, (b) specific capacity normalized by the total weight of the active material as a function of cycle number, (c) electrochemical impedance spectra of various coin cells as indicated, and (d) equivalent circuits used for curve fitting of the EIS data before and after cycling.

inside Si@void@C(N) particles, that is, Si nanoclusters within Si@void@C(N) particles break down along the defect sites during lithiation and delithiation, exposing new surface for fast Li^+ insertion and extraction kinetics and thus the gradually increased capacity. The competition of the aforementioned two mechanisms results in a gradual increase or little decay of the specific capacity in the first several hundreds of cycles, followed by a gradual and obvious decay of the specific capacity in the last several hundreds of cycles, as shown in Figure 8.

https://doi.org/10.1021/acsaem.1c00351
ACS Appl. Energy Mater. XXXX, XXX, XXX–XXX

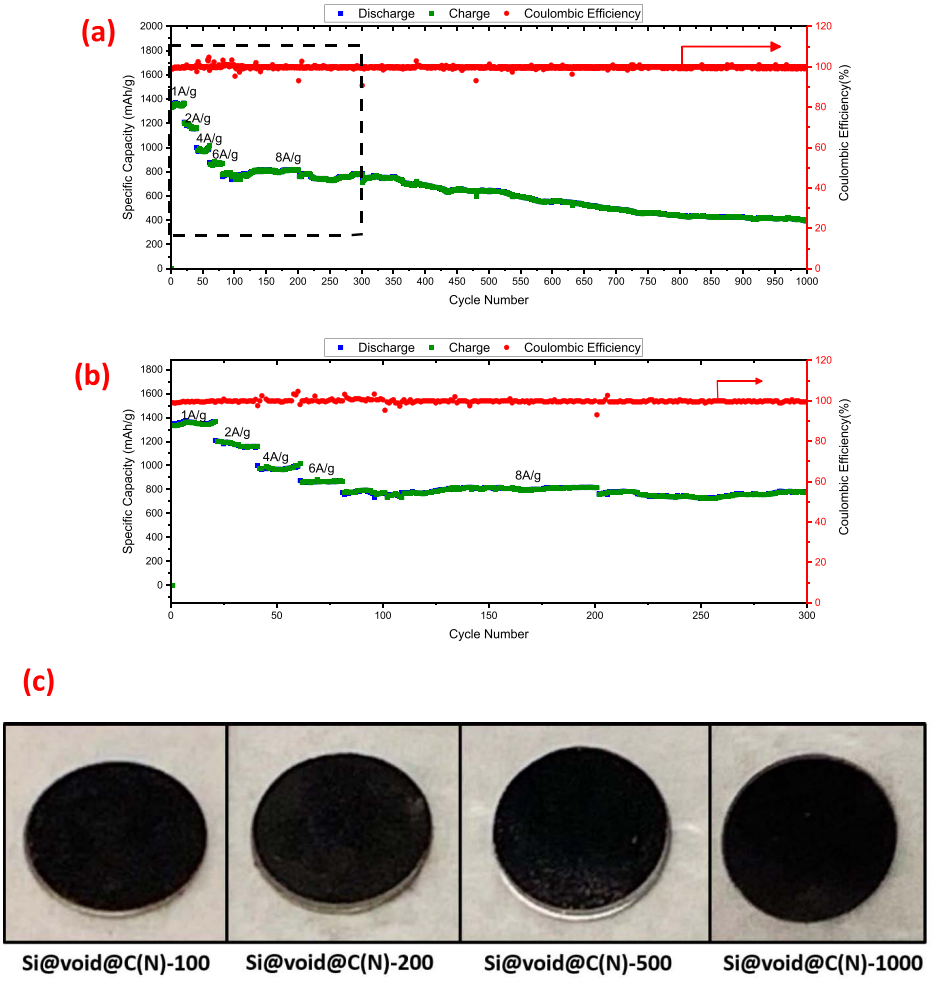

Figure 8. (a) Specific capacity and Coulombic efficiency of Si@void@C(N) coin cells under ultrafast charge/discharge conditions for 1000 cycles, (b) enlarge portion of the first 300 cycles in (a), and (c) photos of the decrimped Si@void@C(N) electrodes after 100, 200, 500, and 1000 cycles at the conditions shown in (a).

Note that Figure 7 has also offered several additional important messages. To achieve direct comparison, all three coin cells in Figure 7 are fabricated with the same active material mass loading of 1.0 mg cm^{-2}, and all cells have the same formation cycles before the rate test: 5 cycles at 0.05 A g^{-1} and 5 cycles at 0.1 A g^{-1}. The mass of the active material in this study refers to the total mass of Si nanoparticles, Si@C(N) particles, and Si@void@C(N) particles in the electrode. In addition, all coin cells are examined with Parstat 4000 for electrochemical impedance measurements at their fresh state and final state after 100 cycles (Figure 7c). As shown in Figure 7a, Si@C(N) has a better cycle stability than Si nanoparticles because the N-doped carbon shell of Si@C(N) can offer facile electron transport for lithiation and delithiation of Si. Moreover, Si@void@C(N) provides better cycle stability than Si@C(N) because the former contains engineered voids to minimize the expansion and shrinkage of Si@void@C(N) themselves and thus a stable SEI layer for repeated lithiation and delithiation. These principles have been observed in many prior studies as summarized in ref 6.

Another important information in Figure 7, particularly for practical applications, is that the total weight of Si@void@C(N) particles should also be taken into account in the specific capacity calculation rather than just the calculation based on the Si mass only. Figure 7b displays the specific capacity normalized by the total weight of the active material in the electrode. In this plot, the Si-nanoparticle coin cell gives the highest specific capacity initially at 1102 mAh g^{-1}, followed by Si@C(N) at 896 mAh g^{-1}, and finally 808 mAh g^{-1} for Si@void@C(N). The discrepancy on specific capacities comes from less Si amount in Si@C(N) and Si@void@C(N), which contain ~70 and 50 wt % Si, respectively. As the current rate doubles to 0.5 A g^{-1} and quadruples to 1.0 A g^{-1}, the specific capacity of Si nanoparticles continuously drops to less than 100 mAh g^{-1} and fails to keep above 200 mAh g^{-1} even after the current is returned back to 0.25 A g^{-1}. Si@C(N) gives better performance than Si nanoparticles, partially recovers the capacity, and achieves 545 mAh g^{-1} at the end of the test, however, still losing 39% of the initial capacity. Si@void@C(N), although having the lowest specific capacity at the beginning due to its smallest Si amount, experiences almost no capacity decay in all stages of current rates. After 100 cycles of the rate performance test, Si@void@C(N) ends up with 93% of capacity retention. These results unambiguously prove the beneficial effects of the carbon coating and engineered voids on the cycle stability and rate capability of Si@void@C. Additionally, it should also be noted that the specific capacity (~800 mAh g^{-1}) offered by Si@void@C(N) is more than 100% that of graphite (~350 mAh g^{-1}) even with the consideration of the total weight of Si@void@C(N).

https://doi.org/10.1021/acsaem.1c00351
ACS Appl. Energy Mater. XXXX, XXX, XXX−XXX

The electrochemical impedance measurements of the three types of materials before and after the rate performance test are shown in Figure 7c, which shed light on why Si@void@C(N) has the best cycle stability from the perspective of impedance analysis. The equivalent circuits used before and after cycling are illustrated in Figure 7d, where R_{el} stands for electrolyte resistance, whereas R_{sei}, R_{int}, and R_{ct} are SEI layer resistance, contact resistance of interphases, and charge-transfer resistance, respectively. CPE_{sei}, CPE_{int}, and CPE_{ct} are the capacitances of the constant phase elements associated with the corresponding resistances mentioned above. Z_w is the Warburg impedance representing the diffusion resistance of Li^+ into the active material. Since there is no SEI layer before any cycling of the cell, the equivalent circuits used for fresh cells contain only two time constants,[58,59] whereas the equivalent circuits for cycled cells have three time constants. Table 3 summarizes the fitted data of various resistances before and after the rate performance test. Before cycling, the interphase resistance of the Si-nanoparticle cell is 571.1 Ω due to silicon's high intrinsic resistivity, whereas Si@C(N) and Si@void@C(N) cells are 130.5 and 73.2 Ω of the interphase resistance, indicating that the conductivity of the electrode material is improved dramatically with the N-doped carbon coating. After 100 cycles of the rate test, the Si-nanoparticle cell exhibits a substantial increase in R_{el} (from 16.9 to 105.6 Ω) caused by the electrolyte degradation because of repeated particle volume expansion and shrinkage and thus repeated formation and collapse of the SEI layer with continuous consumption of the electrolyte. This high R_{el} is accompanied by a high R_{sei} (52.8 Ω) of the Si-nanoparticle cell due to the SEI debris accumulation. Si@C(N) gives better impedance results when compared with Si nanoparticles but still has R_{el} increasing from 10.0 to 53.1 Ω as well as a higher R_{sei} (38.9 Ω) than that of Si@void@C(N) (only 11.0 Ω after 100 cycles). These results suggest that Si@C(N) fails to keep its original structure because of lacking spaces to accommodate the Si volume expansion, leading to increased R_{el} and R_{sei}. In spite of its degradation, Si@C(N) is not as bad as Si nanoparticles, which could be attributed to the partial mechanical constraint from the carbon coating and SiC sites that limit the Si volume expansion to some extent. In sharp contrast, Si@void@C(N) gives the best impedance result after 100 cycles. With the formation of a thin and stable SEI layer, R_{sei} is only 11.0 Ω and there is almost no R_{el} increase, indicating little or no electrolyte degradation. Si@void@C(N) also has the lowest R_{ct} among the three cells. All of these are consistent with the superior capacity retention of Si@void@C(N), suggesting that Si volume expansion and shrinkage is well controlled by creating a N-doped carbon shell and the engineered voids inside the Si@void@C(N) structure. Finally, it is noted that all three cells exhibit some reductions in the interphase resistance (R_{int}) after 100 cycles, which is usually explained by the improved contact between the current collector and the binder system due to expansion of lithiated Si particles.[57]

Table 3. EIS Fitted Results for Si Nanoparticles, Si@C(N), and Si@void@C(N) Before and After 100 Cycles

	nano Si		Si@C(N)		Si@void@C(N)	
	0th	100th	0th	100th	0th	100th
R_{el}	16.9	105.6	10.0	53.1	6.3	7.5
R_{sei}		52.8		38.9		11.0
R_{int}	571.1	448.1	130.5	75.4	73.2	24.6
R_{ct}	2.4	209.0	3.3	173.2	2.3	73.1

2.6. Fast Charge Capability and Long Cycle Life Evaluation. To further explore the electrochemical performance of Si@void@C(N), ultrafast charge capability and long cycle experiments (1000 cycles) are designed and conducted. Figure 8a provides the specific capacity and Coulombic efficiency vs cycle number plot of a Si@void@C(N) cell. Here, the specific capacity is normalized by the Si mass only. As the current rate increases stepwise from 1 to 2, 4, 6, and finally to 8 A g^{-1}, the specific capacity drops to ~1100, ~1000, ~900, and finally to ~800 mAh g^{-1}, respectively. From the enlarged plot in Figure 8b, it can be seen that before 300 cycles there is little or no capacity decay at each level of the current rate. Even at 8 A g^{-1}, the capacity is retained at ~800 mAh g^{-1} for more than 200 cycles. However, after 300 cycles, the specific capacity starts to decrease with the decay rate from 0.02 to 0.12% per cycle in the subsequent cycles, leading to an overall capacity retention of 51% after 925 cycles at 8 A g^{-1}.

Note that at the current density of 8 A g^{-1} and the specific capacity ranging from 800 to 420 mAh g^{-1}, Si@void@C(N) can be charged to the full capacity in 6.0−3.15 min. Such ultrafast charging capability (i.e., charge at the current density of 8 A g^{-1} Si for 925 cycles) exhibited by Si@void@C(N) is among the best high-rate Si anodes reported in the open literature. For example, a high-rate Si anode based on Si nanoparticles has been reported to be capable of 600 cycles at the current density of 5 A g^{-1}.[60] In addition, double-walled Si nanotubes have been proven to exhibit ~600 mAh g^{-1} for 6000 cycles at 7.5 A g^{-1}.[26] Recently, two additional high-rate Si anodes have been synthesized via very elaborated procedures, one study using HF etching first to create potholes in micron-sized Si particles followed by nano-Cu particle deposition to serve as the catalyst for subsequent carbon nanotube growth on the surface of Si particles[61] and the other study starting with Si nanoparticles coated with the physical vapor deposition Cu layer to serve as the catalyst for subsequent graphene growth on the surface of Cu-coated Si nanoparticles and finally acid etching of the Cu layer to generate graphene-coated Si nanoparticles.[62] Both studies lead to high-rate Si anodes with a specific capacity of 463 mAh g^{-1} at 20 A g^{-1} [61] and 3500 cycles also at 20 A g^{-1}.[62] There are other Si-based particles exhibiting long cycle life but with lower rate capability such as 1000 cycles at 2 A g^{-1},[19,63] 1000 cycles at 1.5 A g^{-1},[12] and 600 cycles at 1.2 A g^{-1}.[64] More detailed comparisons in the ultrafast charging capability between Si@void@C(N) and many outstanding Si-based anodes are provided in Table S1 in which the specific capacity and the mass loading of the active material are also included in the comparisons. In short, it is very clear that Si@void@C(N) is among the best in Si anode designs with ultrafast charging capability.

Because of its capability to withstand a very high current per unit Si mass, we expect Si@void@C(N) to be capable of ultrafast charge without Li plating. To confirm that this is indeed the case, Si@void@C(N) cells are decrimped after different numbers of cycles at 8 A g^{-1}. Figure 8c shows photos of Si@void@C(N) electrodes after 100, 200, 500, and 1000 cycles at 8 A g^{-1}. No discernable Li plating can be observed even after 1000 cycles because there is no shinning metallic deposit on the surface of the black electrode, indicating that Si@void@C(N) is capable of ultrafast charge with a high specific capacity, long cycle life (1000 cycles), and no Li plating. Note that at the current density of 8 A g^{-1} Si, the areal

https://doi.org/10.1021/acsaem.1c00351
ACS Appl. Energy Mater. XXXX, XXX, XXX−XXX

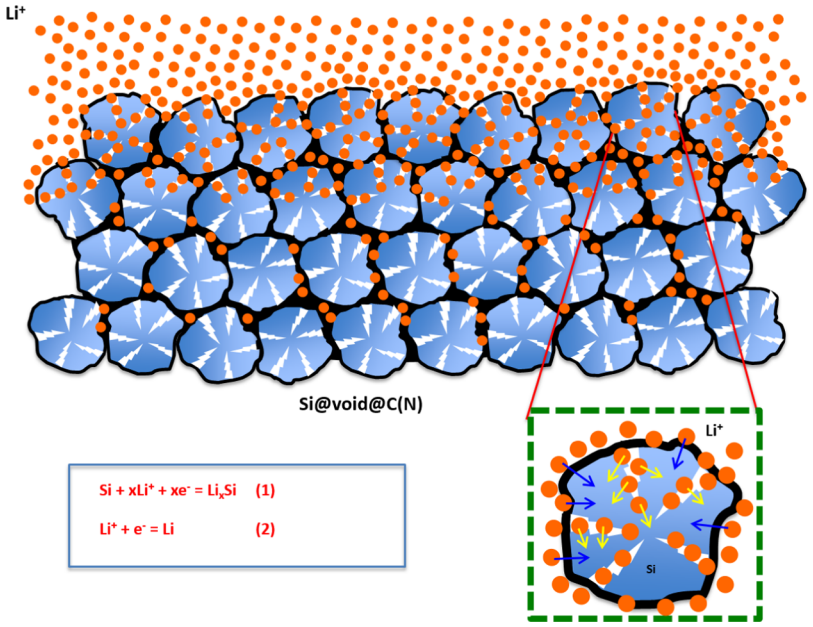

Figure 9. Schematic of a Si@void@C(N) electrode with ultrafast Li-ion insertion and alloying. The enlarged inset shows fast transport of Li^+ ions passing through the porous carbon shell and then entering Si nanoclusters directly or diffusing through the surfaces of nanochannel voids and then laterally into the remaining solids of the Si nanoclusters. Reactions (1) and (2) are two competing reactions for the reduction of Li^+ ions. Figure 1 shows the key components of each Si@void@C(N) particle, and the text shows discussion.

current density for the Si@void@C(N) cell in Figure 8 is 3.4 mA cm^{-2} (i.e., 8 A g^{-1} Si × 0.425 mg Si cm^{-2}). This areal current density is higher than many critical areal current densities above which Li plating occurs in graphite anodes. For instance, it has been shown that Li plating takes place on the surface of MCMB graphite anodes when the areal current density is as low as 0.53, 0.8, and 1.6 mA cm^{-2}.[65] A recent study shows that Li plating occurs on the surface of artificial graphite anodes at 1.0 mA cm^{-2} after 100 cycles.[66] Among all of the reports, the highest critical areal current density for Li plating reported for graphite anodes is between 3.0 and 4.0 mA cm^{-2} (or precisely 3.3 mA cm^{-2}) for the synthetic graphite.[67] Thus, it can be concluded that Si@void@C(N) can avoid Li plating at the highest areal current density exhibited by graphite anodes. In addition, it can be predicted that the critical areal current density for Li plating on the surface of Si@void@C(N) anodes will be higher than that exhibited by the best graphite anodes (<4 mA cm^{-2}) because Si@void@C(N) can be lithiated at 8 A g^{-1} Si without Li plating, whereas the best graphite anode exhibits Li plating when it is lithiated at ~0.45 A g^{-1} graphite.[67]

From the specific capacity viewpoint, Si@void@C(N) has delivered a much higher capacity than graphite anodes under ultrafast charging conditions. A previous study on seven different graphite anodes[68] has shown that the specific capacities of graphite anodes vary with graphite specific surface area, particle size, and morphology, but all of them have the specific capacities below 93 mAh g^{-1} at the current density of 1.85 A g^{-1} graphite (12 min charge) and below 74 mAh g^{-1} at 3.7 A g^{-1} graphite (6 min charge) even though their specific capacity is about 340 mAh g^{-1} at the current density of 0.037 A g^{-1} graphite. Thus, the specific capacities of Si@void@C(N) ranging from ~800 to 420 mAh g^{-1} at 8 A g^{-1} Si are more than 10.5 and 5.5 times the specific capacity (74 mAh g^{-1}) of the best graphite anode at 3.7 A g^{-1} graphite.

We attribute the ultrafast charge capability to the unique design of Si@void@C(N), particularly the presence of nanochannel voids. This hypothesis is illustrated in Figure 9. As shown schematically in Figure 9, ultrafast charging means that a large number of Li^+ ions migrate across the porous membrane from the counter electrode to the Si@void@C(N) electrode. These Li^+ ions should alloy with the Si nanoclusters inside Si@void@C(N) particles and consume a large number of electrons via reaction (1) very quickly. If Li^+ ions cannot alloy with the Si nanoclusters quickly or a large number of electrons are not available for reaction (1), then Li^+ ions will accumulate on the surface of Si@void@C particles, leading to a significant reduction in the electrode potential and even below the lithium potential (Li^+/Li). As a result, Li plating will occur via reaction (2) with dendrite growth which will pose serious problems in terms of reliability and safety of Li-ion batteries.[67,68]

$$Si + Li^+ + xe^- = Li_xSi \quad (1)$$

$$Li^+ + e^- = Li \quad (2)$$

The Si@void@C electrode can avoid the Li plating problem in ultrafast charging because Li^+ ions can transport through the porous carbon shell quickly and then enter the Si nanoclusters through the Si particle surfaces as well as the surfaces of nanochannel voids. It is well known that surface diffusion is several orders of magnitude faster than diffusion inside a solid.[69] Thus, Li^+ ions can diffuse rapidly to the center of the Si nanoclusters through the surfaces of nanochannel voids and then diffuse laterally into the remaining solids of the Si nanoclusters from the surfaces of the nanochannel voids, as shown by the enlarged inset in Figure 9. The porous carbon shell also acts as a superhighway for electrons so that rapid Li alloying with the Si nanoclusters can be accomplished via reaction (1), preventing reaction (2), and thus Li plating from occurring.

https://doi.org/10.1021/acsaem.1c00351
ACS Appl. Energy Mater. XXXX, XXX, XXX−XXX

It should be emphasized that nanochannel voids are critical for the ultrafast charge capability observed for Si@void@C(N) microreactor. Nanochannel voids are very different from the typical spherical or bulky voids in the yolk−shell structure.[12−18] These spherical or bulky voids lead to point contact between the Si yolk and the conductive shell, as schematically shown in Figure S2. As a result of the point contact, yolk−shell nanoparticles can only be charged/discharged with low current densities because of the very limited cross-sectional area for Li-ion transport to the nano-Si core. Indeed, nearly all yolk−shell nanoparticles exhibit charge/discharge capability at the current density $\leq$2.0 A g^{-1}.[12−18] Note that the contact between the Si core and the carbon shell in the Si@void@C(N) microreactor is area contact (Figures 4, 5, and 9), which allows more Li-ion transport to the center of the Si@void@C(N) microreactor. Together, these unique features provide the Si@void@C(N) microreactor with ultrafast charge capability.

It is worthy of mentioning that the ultrafast charge capability of Si@void@C(N) is also demonstrated using experiments with the current density at 6 A g^{-1}. As shown in Figure S3, Si@void@C(N) can be charged to the full capacity in 6−8 min with 500 cycle stability and specific capacities 2−3 times that of graphite anodes, which typically require ∼4 h to be fully charged with only ∼350 mAh g^{-1}. Thus, there is no doubt that Si@void@C(N) developed in this study is capable of ultrafast charge with high specific capacity, long cycle life, and no Li plating.

Finally, it is interesting and important to find out whether nanochannel voids inside Si@void@C(N) particles have minimized or completely prevented the thickness increase of the Si@void@C(N) electrode since it is well known that Si electrodes swell significantly (such as ∼300% increase in the electrode thickness for just one lithiation operation).[70] To study this phenomenon, we decrimped Si@void@C(N) half cells after 75, 520, and 620 cycles at the 1.0 A g^{-1} current density. The average thickness of the electrode (with 15 measurements per electrode using a micrometer) was found to be 26.1 μm before cycles and increase to 33.6, 36.5, and 36.9 μm after 75, 520, and 620 cycles, i.e., 28.7, 39.8, and 41.6% thickness increase after 75, 520, and 620 cycles, respectively. Thus, nanochannel voids inside Si@void@C(N) particles are not sufficient to completely avoid the thickness increase of the Si@void@C(N) electrode but have significantly minimized the thickness increase. Our recent study using in situ electrochemical dilatometry[70] has revealed that the thickness increase of an electrode composed of 70 wt % Si nanoparticles and 30 wt % carbon black is 75% when the lower cutoff voltage is at 0.1 V vs Li^+/Li and ∼300% when the lower cutoff voltage is at 0.01 V vs Li^+/Li after only one cycle. These results indicate that nanochannel voids have drastically reduced the thickness increase in lithiation, but further increase in the volume of nanochannel voids inside Si@void@C(N) particles is needed to completely avoid the thickness increase of the Si@void@C(N) electrode.

Before conclusion, it should be emphasized that although Si@void@C(N) is one of the best performance Si anodes ever reported, it is necessary to conduct further investigations and fundamental analysis on its degradation mechanism. For example, the capacity decay over 1000 cycles (Figure 8) is too large for electric vehicle applications. The understanding of the degradation mechanism(s) and the remedy to address the degradation issue are essential to further improve the properties of Si@void@C(N). Based on the phenomenon of the electrode thickness increase mentioned above, it is anticipated that a further increase in the volume of the engineered nanochannel voids could result in better capacity retention over long cycles. In addition, the voltage profile of the charge/discharge curves of Si@void@C(N), as shown in Figure S4, provide some insight into the problem of gradual degradation as the number of cycles increases. The polarization effect could be seen obviously in this plot with the increased voltage drop at the start of each lithiation cycle and the higher voltage level at the starting point of each delithiation process. The root cause(s) for capacity decay beyond 300 cycles and gradually increased polarization will be investigated in the future to push the Si@void@C(N) performance to the next level.

3. CONCLUSIONS

We have successfully designed and synthesized a Si-based microreactor with Si nanoclusters and nanochannel voids encapsulated by a N-doped carbon shell as a high-performance anode material for Li-ion batteries. Denoted as Si@void@C(N), the microreactor is synthesized through a facile, low cost, and scalable method, composed of three major steps: (1) high-energy ball milling, (2) carbon coating, and (3) partial etching of Si. The half cells made of Si@void@C(N) exhibit high specific capacity, high power, and long cycle life simultaneously. Furthermore, Si@void@C(N) delivers a high initial Coulombic efficiency (91%) due to its relatively low specific surface area (35.18 m^2 g^{-1}) and is able to offer 1100, 1000, 900, and 800 mAh g^{-1} of the specific capacity at the current rate of 2, 4, 6, and 8 A g^{-1}, respectively, with little or no capacity decay at each current level in the first 300 cycles. The cells can also live up to 1000 cycles at the 8 A g^{-1} current density with no Li plating. The ultrafast charge capability and the long cycle life of Si@void@C(N) are attributed to its unique structure features with nanochannel voids. The N-doped carbon coating greatly improves the electric conductivity of the microreactor, while the nanochannel voids enable fast transportation of Li^+ ions into the center of Si nanoclusters, permitting fast alloying of Li^+ ions with Si nanoclusters and avoiding Li plating. The nanochannel voids also provide space to accommodate the volume expansion of Si nanoclusters, while the N-doped carbon coating confines the expansion inward, leading to a stable Si@void@C particle/electrolyte interface for the formation of a stable SEI layer. The elastic sites of a small amount of SiC and $FeSi/FeSi_2$ crystallites act as buffers to assist the carbon shell in mechanical constraint on Si expansion outward, resulting in a stable and intact SEI layer over long cycles and thus long cycle life. With the improvement in the capacity retention over long cycles in the future, Si@void@C(N) has the potential for practical applications.

4. EXPERIMENTAL SECTION

4.1. Material Synthesis. Submicron-sized Si@void@C(N) particles were prepared through three major steps as shown in Figure 1. The synthesis started with micron-sized Si particles (99.5% trace metals basis, Sigma-Aldrich) as the raw material which was sealed in a canister under Ar atmosphere, loaded with steel balls at the charge ratio of 15:1. The raw material was ball-milled for a total of 13 h using a SPEX 8000M Mixer/Mill, with every 1 h ball milling followed by at least 10 min cooling rest before the next 1 h ball milling to avoid overheating. After ball milling of Si particles for 12 h, the carbon precursor, polyacrylonitrile (PAN) powder with a mean particle size of 50 μm (Sigma-Aldrich), was added to the ball-milled Si powder

https://doi.org/10.1021/acsaem.1c00351
ACS Appl. Energy Mater. XXXX, XXX, XXX−XXX

and the Si + PAN mixture was ball-milled for 1 h to mechanically inject the nanostructured Si particles into soft PAN particles. The ball-milled powder mixture was then transferred into a tube furnace and heated to 900 °C for 5 h at the rate of 5 °C min^{-1} under a flowing Ar atmosphere to convert nanostructured Si particles embedded inside a PAN matrix to N-doped carbon-encapsulated Si particles, denoted as Si@C(N). The Si cores inside Si@C(N) particles were then etched away partially using a 0.5 M NaOH solution to create Si@void@C(N) microreactors with nanochannel voids and Si nanoclusters encapsulated by a N-doped carbon shell. Ten volume percent 2-proponal was added to the 0.5 M NaOH solution to improve the wetting of Si by the etchant and thus more uniform etching. The etchant solution was controlled at 47 °C before etching starts. Once the exothermic reaction starts, the temperature will gradually rise up to about 55 °C. The whole etching process was performed for 20 min, followed by three times of DI water washing at room temperature. The etched powder was collected via high-speed centrifuge and filtration and then vacuum-dried at 120 °C for 12 h, denoted as Si@void@C(N) for the subsequent use.

4.2. Material Characterization. JEOL JSM-5900LV SEM (JEOL Ltd., Tokyo, Japan) was used to observe the morphologies, sizes, and structures of ball-milled Si, Si@C(N), and Si@void@C(N) powders. Composition analysis was performed using the EDS system attached to the SEM. Samples were coated with silver via a sputter coater before being transferred into the SEM chamber. To further identify the coating thickness, elemental distribution, and nanochannel voids, JEOL JEM-2100F TEM equipped with a Gatan Imaging Filter system and FEI Talos F200X TEM/STEM with the capability for high-resolution STEM imaging in the Center for Nanoscale Materials (CNM) at Argonne National Laboratory (ANL) were used. Raman measurement of powders at different synthesis steps was performed using a Renishaw inVia confocal Raman microscope with 514 nm of excitation wavelength and a grating of 1800 lines per mm. XRD patterns of the materials were collected using Bruker D2 Phaser with Bragg-Brentano geometry in the 2Θ range of 10−100° with Cu Kα radiation (1.54056 Å). To investigate the surface chemical composition of Si@void@C(N) particles, XPS experiments were performed using Kratos AXIS-165 with monochromatic Al as an X-ray source. High-resolution scans were conducted using pass energy of 20 eV and the C 1s peak of graphitic carbon at 284.5 eV was used for calibration of the energy scale. Further, to determine the SSA of Si powders at different processing stages, BET measurement was performed using a two-channel Nova Quantachrome 2200e surface area and a pore size analyzer.

4.3. Electrochemical Measurements. Si@C(N) and Si@void@C(N) particles were used as active materials and prepared into electrode slurries to fabricate Si@C(N) and Si@void@C(N) coin cells, respectively. For each electrode, the active material, carbon black (MTI Super P conductive carbon black, >99%), and poly(acrylic acid) (PAA, Sigma-Aldrich) binder were mixed together in *N*-methyl-2-pyrrolidone (NMP) solvent at the weight ratio of 6:3:1. The mixture was sonicated for 8 min and then further mixed using a Thinky Mixer (250 rpm for 5 min). This mixing procedure was repeated three times to achieve an extremely uniform state. The electrode slurries were painted onto copper foils and vacuum-dried at 120 °C for 12 h. Half cells in CR2032 coin cell format were fabricated using the dried electrode with a lithium metal chip as the counter electrode and Celgard 2325 membrane as the separator. The active material loading is controlled as 1 mg cm^{-2} for the comparison group of commercial nano-Si, Si@C(N), and Si@void@C(N), while the experiments for 1000 cycles at high current rates use electrodes with the active mass loading ranging from 0.55 to 0.85 mg cm^{-2}. The membrane was soaked in the electrolyte for 20 min before being assembled into the coin cell. The electrolyte was prepared using 1 M $LiPF_6$ salt in ethylene carbonate (EC)−diethyl carbonate (DEC) (1:1 wt/wt), containing 10 vol % fluoroethylene carbonate (FEC) and 1 vol % vinylene carbonate to improve the cycling stability. A Neware battery test system was used to perform galvanostatic charge/discharge experiments with different protocols. The formation cycle protocol was from 0.01 to 1.0 V at 0.05 A g^{-1} for 5 cycles and then at 0.1 A g^{-1} for 5 cycles. After the formation cycles, testing cycles were performed in the voltage window of 0.1−1.0 V with current densities varying from 0.5 to 8 A g^{-1}. Cells before and after each cycling stage were also analyzed with electrochemical impedance spectroscopy (EIS) using Parstat 4000 (Princeton Applied Research). The frequency range from 100 kHz to 0.1 Hz was used in EIS tests to collect impedance data from a relative broad range while also protecting the batteries for the subsequent charge/discharge tests. For comparison, commercial Si nanoparticles with sizes ranging from 70 to 130 nm from NanoAmor (Figure S5 and purity >99%) were also used to fabricate half cells with all other conditions identical with Si@C(N) and Si@void@C(N) coin cells.

■ ASSOCIATED CONTENT

Supporting Information

The Supporting Information is available free of charge at https://pubs.acs.org/doi/10.1021/acsaem.1c00351.

SEM images, additional charge/discharge cycle data, and electrochemical performance comparison with other reports (PDF)

■ AUTHOR INFORMATION

Corresponding Author

Leon Shaw − *Department of Mechanical, Materials and Aerospace Engineering, Illinois Institute of Technology, Chicago, Illinois 60616, United States;* orcid.org/0000-0002-2170-1573; Email: lshaw2@iit.edu

Authors

Qianran He − *Department of Mechanical, Materials and Aerospace Engineering, Illinois Institute of Technology, Chicago, Illinois 60616, United States*

Maziar Ashuri − *Department of Mechanical, Materials and Aerospace Engineering, Illinois Institute of Technology, Chicago, Illinois 60616, United States*

Yuzi Liu − *Center for Nanoscale Materials, Argonne National Laboratory, Lemont, Illinois 60439, United States*

Bingyu Liu − *Department of Mechanical, Materials and Aerospace Engineering, Illinois Institute of Technology, Chicago, Illinois 60616, United States*

Complete contact information is available at: https://pubs.acs.org/10.1021/acsaem.1c00351

Author Contributions

L.S. proposed the concept. Q.H. and L.S. designed the experiments, interpreted results, conceived mechanisms, and wrote the manuscript. Q.H., M.A., and B.L. carried out experiments with the help of Y.L. in the TEM work. All of the authors discussed the results and reviewed the manuscript.

Notes

The authors declare the following competing financial interest(s): Three patent applications have been filed (U.S. Patent Application #16/646,252; China Patent Application #201980007509.X; and EU Patent Application #19741670.4) for design of nano-channel shaped voids and the method to create Si micro-reactors with nano-channel shaped voids.

■ ACKNOWLEDGMENTS

Q.H. acknowledges Tang Fellowship, while M.A., B.L., and L.S. are grateful to the Rowe Family Endowment Fund. Further, this work was partially supported by the U.S. National Science Foundation (NSF) with the Award Number CMMI-1660572. The use of the Center for Nanoscale Materials (CNM) was

supported by the U.S. Department of Energy, Office of Science, Office of Basic Energy Sciences, under Contract No. DE-AC02-06CH11357.

REFERENCES

(1) Dunn, B.; Kamath, H.; Tarascon, J.-M. Electrical Energy Storage for the Grid: A Battery of Choices. *Science* **2011**, *334*, 928−935.
(2) Ashuri, M.; He, Q.; Shi, Z.; Chen, C.; Yao, W.; Kaduk, J.; Segre, C.; Shaw, L. Long-Term Cycle Behavior of Nano-$LiCoO_2$ and Its Postmortem Analysis. *J. Phys. Chem. C* **2019**, *123*, 3299−3308.
(3) Goodenough, J. B.; Park, K.-S. The Li-Ion Rechargeable Battery: A Perspective. *J. Am. Chem. Soc.* **2013**, *135*, 1167−1176.
(4) Chan, C. K.; Peng, H.; Liu, G.; McIlwrath, K.; Zhang, X. F.; Huggins, R. A.; Cui, Y. High-performance lithium battery anodes using silicon nanowires. *Nat. Nanotechnol.* **2008**, *3*, 31−35.
(5) Sun, Y.; Liu, N.; Cui, Y. Promises and challenges of nanomaterials for lithium-based rechargeable batteries. *Nat. Energy* **2016**, *1*, No. 16071.
(6) Ashuri, M.; He, Q.; Shaw, L. L. Silicon as a potential anode material for Li-ion batteries: where size, geometry and structure matter. *Nanoscale* **2016**, *8*, 74−103.
(7) Wu, Z.-H.; Yang, J.-Y.; Yu, B.; Shi, B.-M.; Zhao, C.-R.; Yu, Z.-L. Self-healing alginate−carboxymethyl chitosan porous scaffold as an effective binder for silicon anodes in lithium-ion batteries. *Rare Met.* **2019**, *38*, 832−839.
(8) Zhang, T.; Gao, J.; Zhang, H. P.; Yang, L. C.; Wu, Y. P.; Wu, H. Q. Preparation and electrochemical properties of core-shell Si/SiO nanocomposite as anode material for lithium ion batteries. *Electrochem. Commun.* **2007**, *9*, 886−890.
(9) Hwa, Y.; Kim, W.-S.; Hong, S.-H.; Sohn, H.-J. High capacity and rate capability of core−shell structured nano-Si/C anode for Li-ion batteries. *Electrochim. Acta* **2012**, *71*, 201−205.
(10) Huang, X.; Yang, J.; Mao, S.; Chang, J.; Hallac, P. B.; Fell, C. R.; Metz, B.; Jiang, J.; Hurley, P. T.; Chen, J. Controllable Synthesis of Hollow Si Anode for Long-Cycle-Life Lithium-Ion Batteries. *Adv. Mater.* **2014**, *26*, 4326−4332.
(11) Ashuri, M.; He, Q.; Liu, Y.; Zhang, K.; Emani, S.; Sawicki, M. S.; Shamie, J. S.; Shaw, L. L. Hollow Silicon Nanospheres Encapsulated with a Thin Carbon Shell: An Electrochemical Study. *Electrochim. Acta* **2016**, *215*, 126−141.
(12) Liu, N.; Wu, H.; McDowell, M. T.; Yao, Y.; Wang, C.; Cui, Y. A yolk-shell design for stabilized and scalable Li-ion battery alloy anodes. *Nano Lett.* **2012**, *12*, 3315−3321.
(13) Park, Y.; Choi, N.-S.; Park, S.; Woo, S. H.; Sim, S.; Jang, B. Y.; Oh, S. M.; Park, S.; Cho, J.; Lee, K. T. Si-Encapsulating Hollow Carbon Electrodes via Electroless Etching for Lithium-Ion Batteries. *Adv. Energy Mater.* **2013**, *3*, 206−212.
(14) Yang, L. Y.; Li, H. Z.; Liu, J.; Sun, Z. Q.; Tang, S. S.; Lei, M. Dual yolk-shell structure of carbon and silica-coated silicon for high-performance lithium-ion batteries. *Sci. Rep.* **2015**, *5*, No. 10908.
(15) Xie, J.; Tong, L.; Su, L.; Xu, Y.; Wang, L.; Wang, Y. Core-shell yolk-shell Si@C@Void@C nanohybrids as advanced lithium ion battery anodes with good electronic conductivity and corrosion resistance. *J. Power Sources* **2017**, *342*, 529−536.
(16) Pan, L.; Wang, H.; Gao, D.; Chen, S.; Tan, L.; Li, L. Facile synthesis of yolk−shell structured Si−C nanocomposites as anodes for lithium-ion batteries. *Chem. Commun.* **2014**, *50*, 5878−5880.
(17) Li, X.; Meduri, P.; Chen, X.; Qi, W.; Engelhard, M. H.; Xu, W.; Ding, F.; Xiao, J.; Wang, W.; Wang, C.; Zhang, J.-G.; Liu, J. Hollow core-shell structured porous Si-C nanocomposites for Li-ion battery anodes. *J. Mater. Chem.* **2012**, *22*, 11014−11017.
(18) Zhou, X.-y.; Tang, J.-j.; Yang, J.; Xie, J.; Ma, L.-l. Silicon@carbon hollow core−shell heterostructures novel anode materials for lithium ion batteries. *Electrochim. Acta* **2013**, *87*, 663−668.
(19) Shen, C.; Fang, X.; Ge, M.; Zhang, A.; Liu, Y.; Ma, Y.; Mecklenburg, M.; Nie, X.; Zhou, C. Hierarchical carbon-coated ball-milled silicon: synthesis and applications in free-standing electrodes and high-voltage full lithium-ion batteries. *ACS Nano* **2018**, *12*, 6280−6291.
(20) Liu, N.; Lu, Z.; Zhao, J.; McDowell, M. T.; Lee, H.-W.; Zhao, W.; Cui, Y. A pomegranate-inspired nanoscale design for large-volume-change lithium battery anodes. *Nat. Nanotechnol.* **2014**, *9*, 187−192.
(21) An, Y.; Fei, H.; Zeng, G.; Ci, L.; Xiong, S.; Feng, J.; Qian, Y. Green, Scalable, and Controllable Fabrication of Nanoporous Silicon from Commercial Alloy Precursors for High-Energy Lithium-Ion Batteries. *ACS Nano* **2018**, *12*, 4993−5002.
(22) Yi, R.; Dai, F.; Gordin, M. L.; Chen, S.; Wang, D. Micro-sized Si-C Composite with Interconnected Nanoscale Building Blocks as High-Performance Anodes for Practical Application in Lithium-Ion Batteries. *Adv. Energy Mater.* **2013**, *3*, 295−300.
(23) Tian, H.; Tan, X.; Xin, F.; Wang, C.; Han, W. Micro-sized nano-porous Si/C anodes for lithium ion batteries. *Nano Energy* **2015**, *11*, 490−499.
(24) Cui, L.-F.; Ruffo, R.; Chan, C. K.; Peng, H.; Cui, Y. Crystalline-Amorphous Core−Shell Silicon Nanowires for High Capacity and High Current Battery Electrodes. *Nano Lett.* **2009**, *9*, 491−495.
(25) Ge, M.; Rong, J.; Fang, X.; Zhou, C. Porous Doped Silicon Nanowires for Lithium Ion Battery Anode with Long Cycle Life. *Nano Lett.* **2012**, *12*, 2318−2323.
(26) Wu, H.; Chan, G.; Choi, J. W.; Ryu, I.; Yao, Y.; McDowell, M. T.; Lee, S. W.; Jackson, A.; Yang, Y.; Hu, L.; Cui, Y. Stable cycling of double-walled silicon nanotube battery anodes through solid-electrolyte interphase control. *Nat. Nanotechnol.* **2012**, *7*, 310−315.
(27) Song, T.; Xia, J.; Lee, J.-H.; Lee, D. H.; Kwon, M.-S.; Choi, J.-M.; Wu, J.; Doo, S. K.; Chang, H.; Park, W. I.; Zang, D. S.; Kim, H.; Huang, Y.; Hwang, K.-C.; Rogers, J. A.; Paik, U. Arrays of Sealed Silicon Nanotubes As Anodes for Lithium Ion Batteries. *Nano Lett.* **2010**, *10*, 1710−1716.
(28) Lee, D. J.; Lee, H.; Ryou, M.-H.; Han, G.-B.; Lee, J.-N.; Song, J.; Choi, J.; Cho, K. Y.; Lee, Y. M.; Park, J.-K. Electrospun Three-Dimensional Mesoporous Silicon Nanofibers as an Anode Material for High-Performance Lithium Secondary Batteries. *ACS Appl. Mater. Interfaces* **2013**, *5*, 12005−12010.
(29) Xue, L.; Fu, K.; Li, Y.; Xu, G.; Lu, Y.; Zhang, S.; Toprakci, O.; Zhang, X. Si/C composite nanofibers with stable electric conductive network for use as durable lithium-ion battery anode. *Nano Energy* **2013**, *2*, 361−367.
(30) Li, Y.; Yan, K.; Lee, H.-W.; Lu, Z.; Liu, N.; Cui, Y. Growth of conformal graphene cages on micrometre-sized silicon particles as stable battery anodes. *Nat. Energy* **2016**, *1*, No. 15029.
(31) Ko, M.; Chae, S.; Ma, J.; Kim, N.; Lee, H.-W.; Cui, Y.; Cho, J. Scalable synthesis of silicon-nanolayer-embedded graphite for high-energy lithium-ion batteries. *Nat. Energy* **2016**, *1*, No. 16113.
(32) Ryu, J.; Hong, D.; Shin, M.; Park, S. Multiscale Hyperporous Silicon Flake Anodes for High Initial Coulombic Efficiency and Cycle Stability. *ACS Nano* **2016**, *10*, 10589−10597.
(33) Guo, F.; Chen, C.; Kang, T.; Wang, Y.; Liu, C.; Shen, Y.; Lu, W.; Chen, L. Silicon-Loaded Lithium-Carbon Composite Microspheres as Lithium Secondary Battery Anodes. *Acta Phys.-Chim. Sin.* **2019**, *35*, 1365−1371.
(34) Ren, R.; Yang, Z.; Shaw, L. L. Polymorphic transformation and powder characteristics of TiO_2 during high energy milling. *J. Mater. Sci.* **2000**, *35*, 6015−6026.
(35) Yang, Z.-G.; Shaw, L. L. Synthesis of nanocrystalline SiC at ambient temperature through high energy reaction milling. *Nanostruct. Mater.* **1996**, *7*, 873−886.
(36) Shaw, L. L.; Yang, Z.; Ren, R. Mechanically Enhanced Reactivity of Silicon for the Formation of Silicon Nitride Composites. *J. Am. Ceram. Soc.* **1998**, *81*, 760−764.
(37) Ren, R.; Yang, Z.; Shaw, L. L. Synthesis of nanostructured silicon carbide through an integrated mechanical and thermal activation process. *J. Am. Ceram. Soc.* **2002**, *85*, 819−827.
(38) Gao, M.; Wang, D.; Zhang, X.; Pan, H.; Liu, Y.; Liang, C.; Shang, C.; Guo, Z. A hybrid Si@$FeSi_y$/SiO_x anode structure for high

https://doi.org/10.1021/acsaem.1c00351
ACS Appl. Energy Mater. XXXX, XXX, XXX−XXX

performance lithium-ion batteries via ammonia-assisted one-pot synthesis. *J. Mater. Chem. A* **2015**, *3*, 10767−10776.
(39) Han, H. K.; Loka, C.; Yang, Y. M.; Kim, J. H.; Moon, S. W.; Cho, J. S.; Lee, K.-S. High capacity retention Si/silicide nanocomposite anode materials fabricated by high-energy mechanical milling for lithium-ion rechargeable batteries. *J. Power Sources* **2015**, *281*, 293−300.
(40) Sun, X.; Shao, C.; Zhang, F.; Li, Y.; Wu, Q.-H.; Yang, Y. SiC Nanofibers as Long-Life Lithium-Ion Battery Anode Materials. *Front. Chem.* **2018**, *6*, No. 166.
(41) Kapteijn, F.; Moulijn, J. A.; Matzner, S.; Boehm, H. P. The development of nitrogen functionality in model chars during gasification in CO_2 and O_2. *Carbon* **1999**, *37*, 1143−1150.
(42) Jeong, H. M.; Lee, J. W.; Shin, W. H.; Choi, Y. J.; Shin, H. J.; Kang, J. K.; Choi, J. W. Nitrogen-Doped Graphene for High-Performance Ultracapacitors and the Importance of Nitrogen-Doped Sites at Basal Planes. *Nano Lett.* **2011**, *11*, 2472−2477.
(43) Kong, J.; Yee, W. A.; Yang, L.; Wei, Y.; Phua, S. L.; Ong, H. G.; Ang, J. M.; Li, X.; Lu, X. Highly electrically conductive layered carbon derived from polydopamine and its functions in SnO_2-based lithium ion battery anodes. *Chem. Commun.* **2012**, *48*, 10316−10318.
(44) Yang, J.; Takeda, Y.; Imanishi, N.; Capiglia, C.; Xie, J. Y.; Yamamoto, O. SiO_x-based anodes for secondary lithium batteries. *Solid State Ionics* **2002**, *152*−*153*, 125−129.
(45) Xu, C.; Lindgren, F.; Philippe, B.; Gorgoi, M.; Björefors, F.; Edström, K.; Gustafsson, T. Improved Performance of the Silicon Anode for Li-Ion Batteries: Understanding the Surface Modification Mechanism of Fluoroethylene Carbonate as an Effective Electrolyte Additive. *Chem. Mater.* **2015**, *27*, 2591−2599.
(46) Jin, Y.; Kneusels, N.-J. H.; Marbella, L. E.; Castillo-Martínez, E.; Magusin, P. C. M. M.; Weatherup, R. S.; Jónsson, E.; Liu, T.; Paul, S.; Grey, C. P. Understanding Fluoroethylene Carbonate and Vinylene Carbonate Based Electrolytes for Si Anodes in Lithium Ion Batteries with NMR Spectroscopy. *J. Am. Chem. Soc.* **2018**, *140*, 9854−9867.
(47) Zhang, X.; Kostecki, R.; Richardson, T. J.; Pugh, J. K.; Ross, P. N. Electrochemical and Infrared Studies of the Reduction of Organic Carbonates. *J. Electrochem. Soc.* **2001**, *148*, A1341−A1345.
(48) Peled, E.; Menkin, S. Review—SEI: Past, Present and Future. *J. Electrochem. Soc.* **2017**, *164*, A1703−A1719.
(49) Chen, X.; Li, X.; Ding, F.; Xu, W.; Xiao, J.; Cao, Y.; Meduri, P.; Liu, J.; Graff, G. L.; Zhang, J.-G. Conductive Rigid Skeleton Supported Silicon as High-Performance Li-Ion Battery Anodes. *Nano Lett.* **2012**, *12*, 4124−4130.
(50) Xie, J.; Wang, G.; Huo, Y.; Zhang, S.; Cao, G.; Zhao, X. Nanostructured silicon spheres prepared by a controllable magnesiothermic reduction as anode for lithium ion batteries. *Electrochim. Acta* **2014**, *135*, 94−100.
(51) Magasinski, A.; Dixon, P.; Hertzberg, B.; Kvit, A.; Ayala, J.; Yushin, G. High-performance lithium-ion anodes using a hierarchical bottom-up approach. *Nat. Mater.* **2010**, *9*, 353−358.
(52) Obrovac, M. N.; Christensen, L. Structural Changes in Silicon Anodes during Lithium Insertion/Extraction. *Electrochem. Solid-State Lett.* **2004**, *7*, A93−A96.
(53) Li, J.; Dahn, J. R. An In Situ X-Ray Diffraction Study of the Reaction of Li with Crystalline Si. *J. Electrochem. Soc.* **2007**, *154*, A156−A161.
(54) Lee, W. J.; Hwang, T. H.; Hwang, J. O.; Kim, H. W.; Lim, J.; Jeong, H. Y.; Shim, J.; Han, T. H.; Kim, J. Y.; Choi, J. W.; Kim, S. O. N-doped graphitic self-encapsulation for high performance silicon anodes in lithium-ion batteries. *Energy Environ. Sci.* **2014**, *7*, 621−626.
(55) Jung, D. S.; Hwang, T. H.; Park, S. B.; Choi, J. W. Spray Drying Method for Large-Scale and High-Performance Silicon Negative Electrodes in Li-Ion Batteries. *Nano Lett.* **2013**, *13*, 2092−2097.
(56) Zhou, X.-y.; Tang, J.-j.; Yang, J.; Zou, Y.-l.; Wang, S.-c.; Xie, J.; Ma, L.-l. Effect of polypyrrole on improving electrochemical performance of silicon based anode materials. *Electrochim. Acta* **2012**, *70*, 296−303.
(57) Yang, X.; Wen, Z.; Xu, X.; Lin, B.; Huang, S. Nanosized silicon-based composite derived by in situ mechanochemical reduction for lithium ion batteries. *J. Power Sources* **2007**, *164*, 880−884.
(58) Zhang, Y.-C.; You, Y.; Xin, S.; Yin, Y.-X.; Zhang, J.; Wang, P.; Zheng, X.-s.; Cao, F.-F.; Guo, Y.-G. Rice husk-derived hierarchical silicon/nitrogen-doped carbon/carbon nanotube spheres as low-cost and high-capacity anodes for lithium-ion batteries. *Nano Energy* **2016**, *25*, 120−127.
(59) Guo, J.; Sun, A.; Chen, X.; Wang, C.; Manivannan, A. Cyclability study of silicon−carbon composite anodes for lithium-ion batteries using electrochemical impedance spectroscopy. *Electrochim. Acta* **2011**, *56*, 3981−3987.
(60) Zhou, X.; Han, K.; Jiang, H.; Liu, Z.; Zhang, Z.; Ye, H.; Liu, Y. High-Rate and Long-Cycle Silicon/Porous Nitrogen-Doped Carbon Anode via a Low-Cost Facile Pre-Template-Coating Approach for Li-ion Batteries. *Electrochim. Acta* **2017**, *245*, 14−24.
(61) Zhang, Z.; Han, X.; Li, L.; Su, P.; Huang, W.; Wang, J.; Xu, J.; Li, C.; Chen, S.; Yang, Y. Tailoring the interfaces of silicon/carbon nanotube for high rate lithium-ion battery anodes. *J. Power Sources* **2020**, *450*, No. 227593.
(62) Ding, X.; Wang, Y. Bilayer-graphene-coated Si nanoparticles as advanced anodes for high-rate lithium-ion batteries. *Electrochim. Acta* **2020**, *329*, No. 134975.
(63) Shen, C.; Fang, X.; Ge, M.; Zhang, A.; Liu, Y.; Ma, Y.; Mecklenburg, M.; Nie, X.; Zhou, C. Hierarchical Carbon-Coated Ball-Milled Silicon: Synthesis and Applications in Free-Standing Electrodes and High-Voltage Full Lithium-Ion Batteries. *ACS Nano* **2018**, *12*, 6280−6291.
(64) Yi, R.; Dai, F.; Gordin, M. L.; Sohn, H.; Wang, D. Influence of Silicon Nanoscale Building Blocks Size and Carbon Coating on the Performance of Micro-Sized Si−C Composite Li-Ion Anodes. *Adv. Energy Mater.* **2013**, *3*, 1507−1515.
(65) Zhang, S. S.; Xu, K.; Jow, T. R. Study of the charging process of a $LiCoO_2$-based Li-ion battery. *J. Power Sources* **2006**, *160*, 1349−1354.
(66) Zhang, P.; Yuan, T.; Pang, Y.; Peng, C.; Yang, J.; Ma, Z.-F.; Zheng, S. Influence of Current Density on Graphite Anode Failure in Lithium-Ion Batteries. *J. Electrochem. Soc.* **2019**, *166*, A5489−A5495.
(67) Gallagher, K. G.; Trask, S. E.; Bauer, C.; Woehrle, T.; Lux, S. F.; Tschech, M.; Lamp, P.; Polzin, B. J.; Ha, S.; Long, B.; Wu, Q.; Lu, W.; Dees, D. W.; Jansen, A. N. Optimizing Areal Capacities through Understanding the Limitations of Lithium-Ion Electrodes. *J. Electrochem. Soc.* **2016**, *163*, A138−A149.
(68) Sivakkumar, S. R.; Nerkar, J. Y.; Pandolfo, A. G. Rate capability of graphite materials as negative electrodes in lithium-ion capacitors. *Electrochim. Acta* **2010**, *55*, 3330−3335.
(69) Shewmon, P. G. *Diffusion in Solids*; Springer International Publishing, 2016.
(70) Prado, A. Y. R.; Rodrigues, M.-T. F.; Trask, S. E.; Shaw, L.; Abraham, D. P. Electrochemical Dilatometry of Si-bearing Electrodes: Dimensional Changes and Experimental Design. *J. Electrochem. Soc.* **2020**, *167*, No. 160551.

https://doi.org/10.1021/acsaem.1c00351
ACS Appl. Energy Mater. XXXX, XXX, XXX−XXX